Tenth International Conference on Computational Fluid Dynamics (ICCFD10), Barcelona, Spain, July 9-13, 2018

ICCFD10-009

Multi-Fidelity Surrogate Models for Flutter Database Generation

Markus Peer Rumpfkeil[1] and Philip Beran[2]

[1] Department of Mechanical and Aerospace Engineering, University of Dayton, USA
[2] U.S. Air Force Research Laboratory, Wright-Patterson Air Force Base, USA
Corresponding author: Markus.Rumpfkeil@udayton.edu

Abstract: In this paper multi-fidelity surrogate (MFS) models of critical flutter dynamic pressures as a function of Mach number, angle of attack and thickness to chord ratio are constructed in lieu of solely using computationally expensive high-fidelity engineering analyses. Once an accurate MFS is constructed it can be used for evaluating a large number of designs for design space exploration as well as of Monte-Carlo samples for uncertainty quantification. To demonstrate that accurate MFS models can be obtained at lower computational cost than high-fidelity ones the well known AGARD 445.6 dynamic aeroelastic test case model will be employed. The highest and lowest fidelity levels considered are Euler and panel solutions, respectively, all combined with a modal structural solver.

Keywords: Multi-fidelity, Surrogate Model, Kriging, Flutter, Aeroelastic Simulations

1 Motivation and Background

Aeroelastic flutter can be a dangerous phenomenon encountered in flexible structures subjected to aerodynamic forces such as aircraft, buildings, and bridges. Flutter occurs as a result of interactions between aerodynamics, stiffness, and inertial forces on a structure caused by positive feedback between the body's deflection and the force exerted by the fluid flow. The implicit assumption for aircraft flutter is that the most critical case at any given Mach number will occur at sea level conditions since the dynamic pressure is highest there. However, Bendiksen [1, 2] presents a counterexample involving a generic swept wing representative for a transport aircraft (called Göttingen or G-wing) in which transonic limit cycle flutter occurs at altitude rather than at sea level. Before detecting such counter-intuitive behaviors often several design stages have already been completed or – in a worst-case scenario – only flight testing will reveal them leading to massive cost and schedule overruns.

Unfortunately, transonic aeroelastic experiments are extremely expensive and there are only a few available in the public domain for validation purposes. One of these are the tests performed in the Langley transonic dynamics tunnel in the early 1960s known as the AGARD 445.6 dynamic aeroelastic test cases [3]. A series of subsonic and transonic flutter data were obtained on different wing models in both air and freon-12. One of these models was denoted "weakened 3" and was made of symmetric NACA 65A004 airfoils with a sweep angle of 45° at the quarter chord line, a semi-span of $0.762\,m$, and a taper ratio of 0.66. The uncambered model was rigidly mounted on the tunnel wall at zero angle of attack thus eliminating any static aeroelastic deformation. In this paper, the experiments on the "weakened 3" model conducted in air are simulated and the considered design space is extended by changing the angle of attack as well as the thickness to chord ratio.

However, computational flutter simulations tend to be very expensive as well since they require unsteady aeroelastic analyses. In order to save computational time while trying to maintain high-fidelity information the construction of highly accurate global surrogate models such as kriging [4, 5, 6, 7, 8] is a very attractive

[0]**Cleared for Public Release, Distribution Unlimited: 88ABW-2018-2557**

option. The kriging surrogate model predicts unknown function values by using stochastic processes on existing training data. Gradient enhanced kriging [9, 10, 11, 12] models are showing great promise as well, however, due to the unavailability of gradient information in some of the employed analysis codes they are not used in this work. For obtaining globally accurate surrogate models as required for design space studies, uncertainty quantification, and flutter databases, kriging surrogate model construction can be enhanced by a dynamic training point selection [13, 14]. Kriging also supports the usage of multi-fidelity training points [15, 16, 12, 17, 18]. The general idea is to combine trends from inexpensive lower fidelity (LF) data (e.g., coarser meshes, less sophisticated models) with interpolations of high-fidelity (HF) data (e.g., finer meshes, better models, experimental data). In addition, multiple local surrogate models can be employed to overcome the limited modeling flexibility of a single global model when there is heterogeneity in the governing function [19, 20, 21]. All these ideas have been implemented as a framework for the construction of multi-fidelity locally optimized surrogate (MFLOS) models [22, 23, 24] which will be used in this paper.

In summary, the goal of this work is to perform aeroelastic flutter simulations of an AGARD 445.6 like geometry at various fidelity levels and then to fuse this multi-fidelity information to give an accurate representation of the underlying design space at a small overall computational cost. Section 2 will describe the computational multi-fidelity aeroelastic flutter analyses in more detail. Section 3 will show results of employing the previously developed MFLOS framework which balances a trade-off between the accuracy (fidelity) of the solution and overall computational time. Section 4 concludes this paper.

2 Aeroelastic Flutter Analysis

In an aeroelastic flutter analysis it is necessary to capture the complex and coupled physical phenomena present in the operating environment and flight regime of modern aircraft. The process begins with the selection of a set of design parameters via a parametric study, surrogate model training point selection, optimizer, etc. A model configuration and geometry generator interprets and maps the given set of design parameters into the required aerodynamic and structural analysis models which also usually require an adequate mesh. Three different analysis fidelity levels are considered which can all predict critical flutter dynamic pressures, q_f. A more detailed description of the overall analysis routines is given in the following subsections.

2.1 Geometry and Meshes

A shared geometric representation of the vehicle in question is central for any multi-fidelity and multi-disciplinary analysis and optimization. Using a single source ensures that the inputs given to each analysis are consistent and aids in the transfer of data between disciplines or fidelity levels. This objective is achieved by using the Computational Aircraft Prototype Synthesis (CAPS) [25] geometry program. Within CAPS exists a parametric, attributed model of the vehicle. The attributes provide logical information required for the generation of analysis inputs. For example, attributes identify the vehicle skins where aeroelastic data transfers take place, symmetry planes for the application of boundary conditions, and bodies to which material properties should be applied. When a shape design parameter is changed, the geometry is regenerated, and analysis models (meshes, properties, etc.) may be requested for various disciplinary analyses at varying levels of fidelity.

The analysis model generation for the employed AGARD 445.6 like geometry proceeds as follows. Note that geometrically only the thickness to chord ratio is varied in this work but the explanation is given for more general modifications. Using the current design parameters, the airfoil cross-sections and the planform shape are determined. Lofting these airfoils provides a solid body representing the outer mold line (OML). These same airfoils also provide the boundaries for defining mid-surface aerodynamic panel models. The computational fluid dynamics (CFD) domain is generated by subtracting the OML solid from a bounding box. Unstructured surface and volume meshes are generated using AFLR4 and AFLR3 [26, 27], respectively.

The internal structure results from intersecting the OML body with a grid representing the structural layout. The layout may have variable topology, though here the topology is held constant, and the shape follows the planform parameterization. The wing skins are extracted from the outer surface of the OML body and a mesh is generated for the finite element analysis (FEA) described in the next subsection. Sample geometric entities used for building the analysis models are presented in Figure 1.

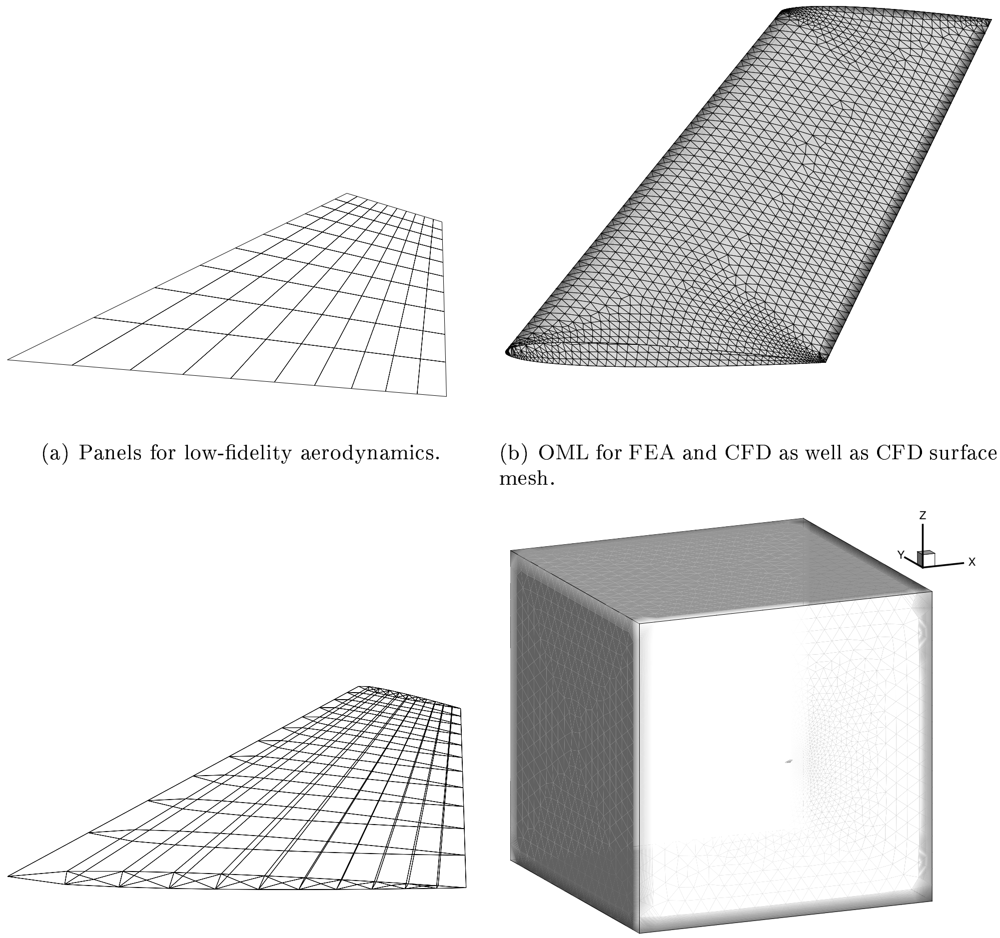

(a) Panels for low-fidelity aerodynamics.

(b) OML for FEA and CFD as well as CFD surface mesh.

(c) Internal structure for FEA.

(d) Fluid domain for CFD.

Figure 1: Representations of the AGARD 445.6 wing for multi-fidelity and multi-disciplinary analyses. Thickness to chord ratio is exaggerated in (b) for better visualization.

2.2 Structural Solver

The employed structural solver is the Automated STRuctural Optimization System (ASTROS) [28]. ASTROS can perform static, modal, and transient linear FEA, and has an internal aerodynamics capability for static and dynamic aeroelastic analyses (see Section 2.3.1). The same structural analysis model feeds all subsequent multi-fidelity aeroelastic flutter analyses described in the next subsection. The structural element thickness is set to $4.65\,mm$ and the material is assumed to be mahogany timber which is isotropic with a Young's modulus of $3.2 \cdot 10^9\,Pa$, shear modulus of $4.1 \cdot 10^8\,Pa$, Poisson's ratio of 0.31, and density of $586\,kg/m^3$. A grid convergence study for the first three modal frequencies resulted in a relatively grid independent solution for the mesh shown in Figure 1(c) containing 279 grid nodes, 242 quadrilateral and 312 triangular elements. The computed first three modal frequencies are $8.9\,Hz$, $32.6\,Hz$ and $38.5\,Hz$ whereas experiments yielded $9.6\,Hz$, $38.2\,Hz$ and $48.3\,Hz$. Note, that the structural properties were tuned to overall match experimental flutter results and not the modal frequencies.

2.3 Flow Solver

As mentioned earlier three different fidelity levels are employed which will be explained in the following subsections.

2.3.1 Low-fidelity: ASTROS

The low-fidelity analysis is performed with the ASTROS package. A flutter analysis requires unsteady aerodynamic influence coefficients to integrate the effects of the structural deformations and the aerodynamic forces in an assessment of dynamic stability. The transfer of loads and displacements between the two disciplines is handled using built-in surface splines [29]. For unsteady subsonic and supersonic applications, the Doublet Lattice Method (DLM) [30] and constant pressure method (CPM) [31] are employed, respectively. The DLM and CPM procedures calculate matrices which provide forces on panels representing the vehicle as a function of deflections at these panels. These matrices are functions of both given Mach number and reduced frequencies which are taken to be 0.005, 0.01, 0.025, 0.05, 0.1, 0.2, 0.4, and 0.8. The one-hundred aerodynamic panels which lead to a number-of-panel independent solution are shown in Figure 1(a).

For the flutter analysis the p-k method is implemented in ASTROS [28] which refines user defined velocities to obtain a high quality flutter response. Here, 30, 50, 75, 90, 100, 110 and 140 percent of the freestream velocity, U_∞, are the user defined velocities at a given Mach number with a reference density of $0.25\,kg/m^3$ and speed of sound of $330\,m/s$. Figure 2 shows the ASTROS simulation results for the dynamic pressure at the flutter threshold, q_f, at zero angle of attack as a function of Mach number together with the experimental data [3].

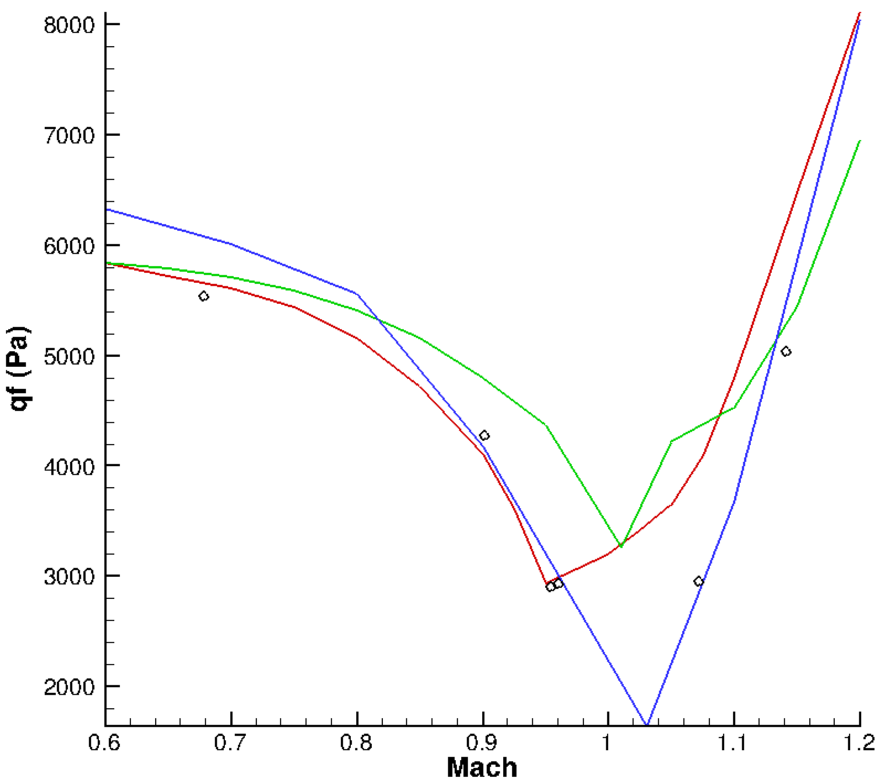

Figure 2: AGARD 445.6 flutter design space with one input. The green, blue and red lines are ASTROS, ZEUS, and inviscid Fun3D results, respectively, and the black circles are experimental data [3].

One can observe a decent agreement between ASTROS (green lines) and the experimental data (black circles).

2.3.2 Medium-fidelity: ZEUS

The medium-fidelity level considered is ZONA's Euler Unsteady Solver (ZEUS) [32] combined with modal structures calculated by ASTROS. ZEUS calculates Euler aerodynamics with or without boundary-layer coupling using a transpiration boundary condition and a Cartesian grid based on a geometry representation similar to ASTROS using 21 span-wise and 61 chord-wise divisions of the wing. The computed unsteady aerodynamic forces are plugged into the frequency domain flutter equation and the solution is obtained using the g-method [32]. Note, that the frequency-domain unsteady aerodynamic forces can be considered as a linearized aerodynamic solution with respect to the structural oscillating amplitude. Thus, they cannot predict nonlinear aeroelastic response such as limit cycle oscillation.

Since the speed of sound was essentially constant during the experimentation (taken to be $330\,m/s$) a non-matched point flutter analysis can be achieved by density iterations using the FIXMACH bulk data entry. Sixteen equidistant density values are specified in the interval $[\frac{\varrho^*}{3}, 3\varrho^*]$, where $\varrho^* = \frac{2q_{guess}}{U_\infty^2}$ and $q_{guess} = 4500\,Pa$. For the solution in the frequency domain via the MKAEROZ bulk data entry the following reduced frequencies are specified: $0.0, 0.06, 0.1, 0.2$ and 0.4.

Figure 2 shows the ZEUS simulation results for q_f, at zero angle of attack as a function of Mach number together with the experimental data [3]. One can see a good agreement between ZEUS (blue lines) and the experimental data (black circles).

2.3.3 High-fidelity: Fun3D

The highest fidelity level considered in this work utilizes NASA's Fully-Unstructured Navier-Stokes 3D (FUN3D) [33] code in Euler mode. FUN3D is a node-centered, implicit, upwind-differencing finite-volume solver. Inviscid wall boundary conditions are applied to the wing outer mold line, and the symmetry plane is modeled with a symmetric boundary condition. The integrated aeroelastic analysis utilizes a modal structural decomposition approach. The implemented linear structural dynamic equations are appropriate for small deflections as occurring during flutter onset [34]. An external FEM solver is used a priori to extract eigenmodes and frequencies. The deflections are represented as linear combination of eigenmodes and typically only a limited set of the "important" eigenmodes are retained. In this case, ASTROS is employed as FEA solver and three mode shapes are included in the dynamic analysis.

The transfer of mode shapes from the structural mesh to the fluid surface mesh is handled by CAPS internally. Representative fluid and structural surface meshes are provided in Figures 1 (b) and (c), respectively. The structural and fluid surfaces are matched by tagging the parametric geometry model with attributes. The nodal displacements from the structural solution are read in through an analysis interface and mapped onto the source geometry, which has knowledge of both the structural and fluid meshes. Each mode shape is then automatically transferred to the fluid surface mesh by interpolating the displacements from the structural mesh through this shared geometry. FUN3D then handles the required volume mesh deformation internally via a linear elastic analogy driven by the surface mesh displacements [34].

A grid convergence study was conducted yielding satisfactory CFD volume meshes with approximately $47,000$ nodes and $250,000$ tetrahedrals. A surface mesh can be seen in Figure 1 (b). The optimized second-order backward difference (BDF2OPT) scheme is employed for temporal discretization. The time step size is selected to have eighteen steps per cycle of the highest modal frequency and the CFL number is set to seventy-five. A maximum of thirty subiterations are used per time step and temporal error tracking is employed. After the first time step, the subiteration sequence is truncated once the continuity residual of the mean flow falls two orders of magnitude below the estimated temporal error. A total of 600 time steps are used to simulate the unsteady aeroelastic behavior with an initial perturbation to "kick" the elastic response. In addition, for non-zero angles of attack 100 preceding time steps are employed to yield the static aeroelastic deflection (by using a critical damping ratio of about one) which is the appropriate starting point for flutter assessment.

A representative plot of C_L versus number of time steps is shown in the left of Figure 3 for the AGARD 445.6 wing at a Mach number of 0.9, zero angle of attack, and dynamic pressure of $4103\,Pa$ which corresponds to the critical flutter pressure at these conditions. The resulting neutral displacement response for the first three modes versus simulation time is shown to the right in the same figure.

In order to be able to determine q_f automatically a bisection method is employed by varying the flutter velocity until a neutral lift coefficient oscillation is achieved. To decide whether the lift coefficient oscillations diverge (value of 1 assigned), converge (-1) or remain neutral (0) the following procedure is used; after linearly detrending the lift data without the first 100 iterations, which are either the static aeroelastic deflection time steps or aphysical due to an adjustment period (which can be seen in the left of Figure 3) a hilbert transformation is performed to compute the instantaneous envelope amplitude. Then a linear curve

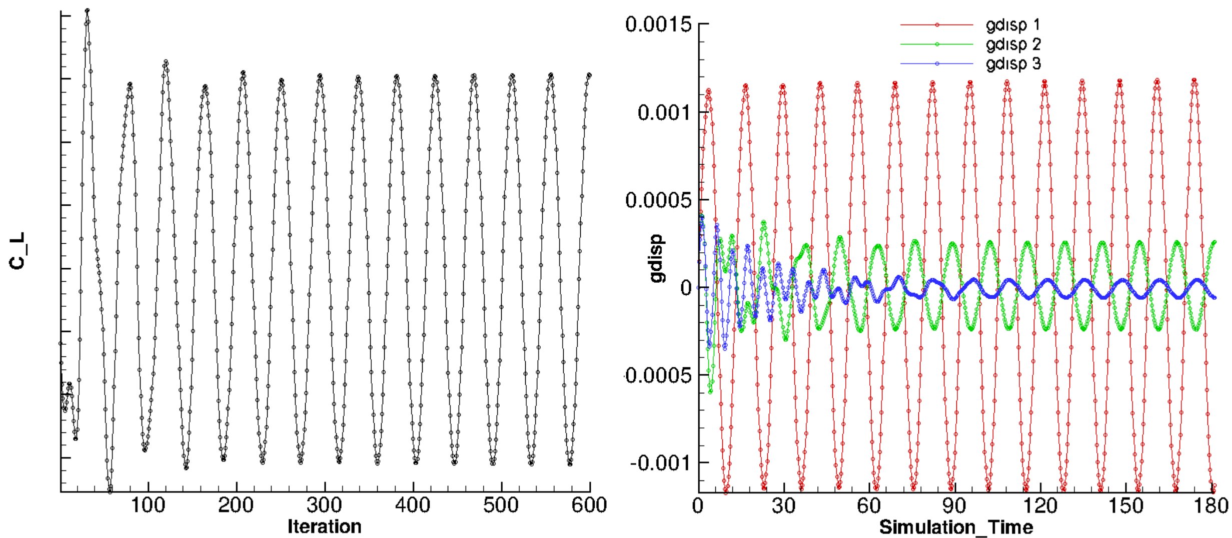

Figure 3: Representative plot of C_L vs number of iterations (left) and a neutral displacement response for first three modes vs simulation time (right).

fit through these amplitudes transformed onto the unit interval is conducted. If the thus determined value of the slope divided by the mean of the amplitudes is larger than 0.03 the response is considered diverging, if it is less than -0.03 converging, and in between it is considered to be neutral as is the case in Figure 3. Some representative plots are given in Figure 4.

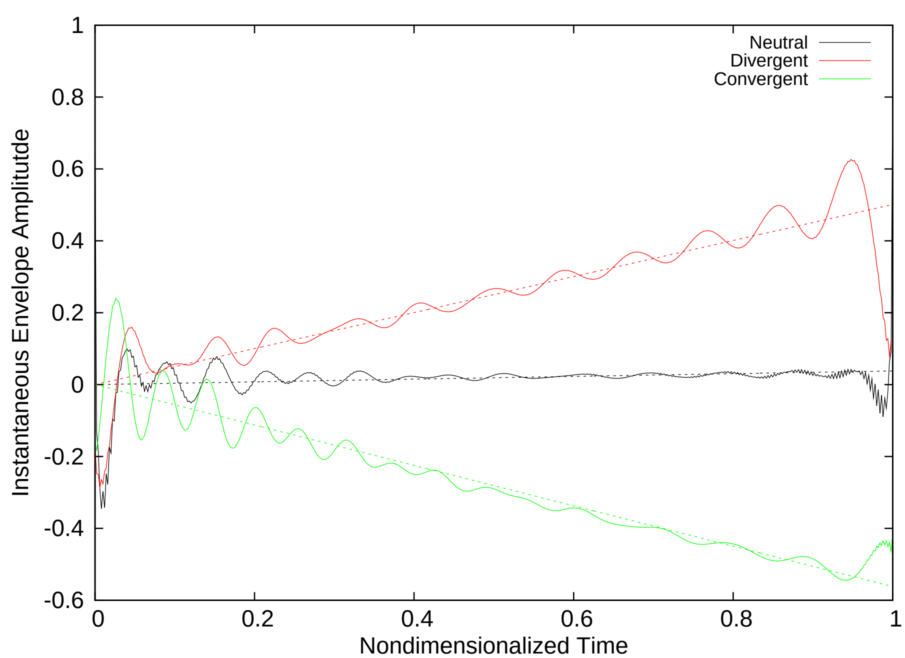

Figure 4: Neutral ($q_\infty = q_f = 4103\,Pa$), diverging ($q_\infty = 4278\,Pa$), and converging ($q_\infty = 3828\,Pa$) lift coefficient oscillations analyzed via hilbert transformation and linear curve fit.

Figure 2 displays results for q_f at zero angle of attack as a function of Mach number showing a good agreement between FUN3D (red lines) and the experimental data.

3 Flutter Databases

The variations of the critical flutter dynamic pressure, q_f, with changes in Mach number ($0.6 \leq M \leq 1.2$) and angle of attack ($0° \leq \alpha \leq 5°$) are studied in Section 3.1. Additionally, in Section 3.2 the variations with thickness to chord ratio ($4\% \leq tc \leq 8\%$) are considered. For each case an "exact" database is obtained from high-fidelity analyses (see Section 2.3.3) on a Cartesian mesh and is used for comparisons and error assessment. One low-fidelity simulation (see Section 2.3.1) runs about 150 times faster, and one medium-fidelity simulation (see Section 2.3.2) runs about 5 times faster than the corresponding high-fidelity simulation on 12 cores.

3.1 Two-dimensional MFS Models

Figure 5 compares the three fidelity levels in the domain of interest if only two inputs, namely Mach number and angle of attack, are varied.

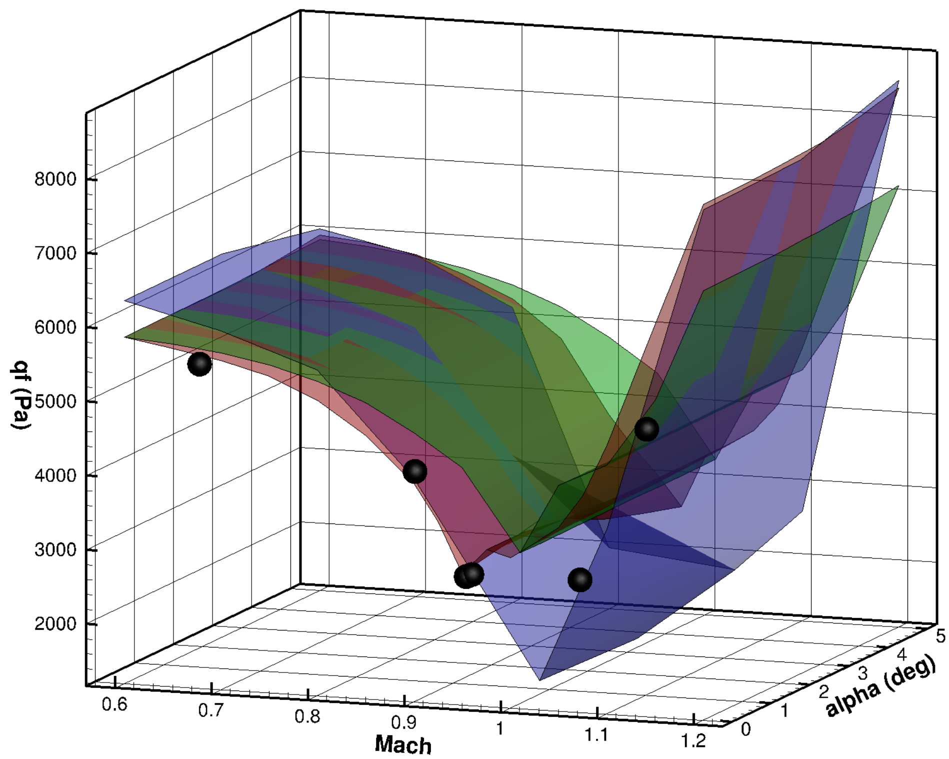

Figure 5: AGARD 445.6 flutter design space with two inputs. The green, blue and red surfaces are ASTROS, ZEUS, and inviscid Fun3D results, respectively, and the black spheres are experimental data [3].

For the HF data a Cartesian mesh of $15 \times 6 = 90$ nodes is employed. One can see that the lower fidelity trends match the high-fidelity ones which is encouraging for the use of a multi-fidelity approach.

All two-dimensional MFS models started with the same five HF training points (4 corners and center of domain). Then the adaptive training point framework [14] added two HF training points per iteration until a maximum amount (25) was reached. When lower fidelity data was used the initial LF locations coincided with all the HF training points and the remaining LF points were picked via latin hypercube sampling subject to a distance constraint [23, 24]. Also, whenever a HF point is added via the dynamic training point algorithm the corresponding lower fidelity point is added to the set as well. Here, 30 and 50 low-fidelity starting points were employed.

Figure 6 shows the exact and MFS kriging model at the end of a simulation (using 25 HF points and 70 LF points). It can be inferred that the MFS model is in good agreement with the exact model and is able to capture the transonic dip behavior very well, demonstrating its ability to model non-smooth functions. One can also observe that the dynamic training point selection clustered HF points in the more varying transonic region as opposed to the relatively flat supersonic and subsonic regions.

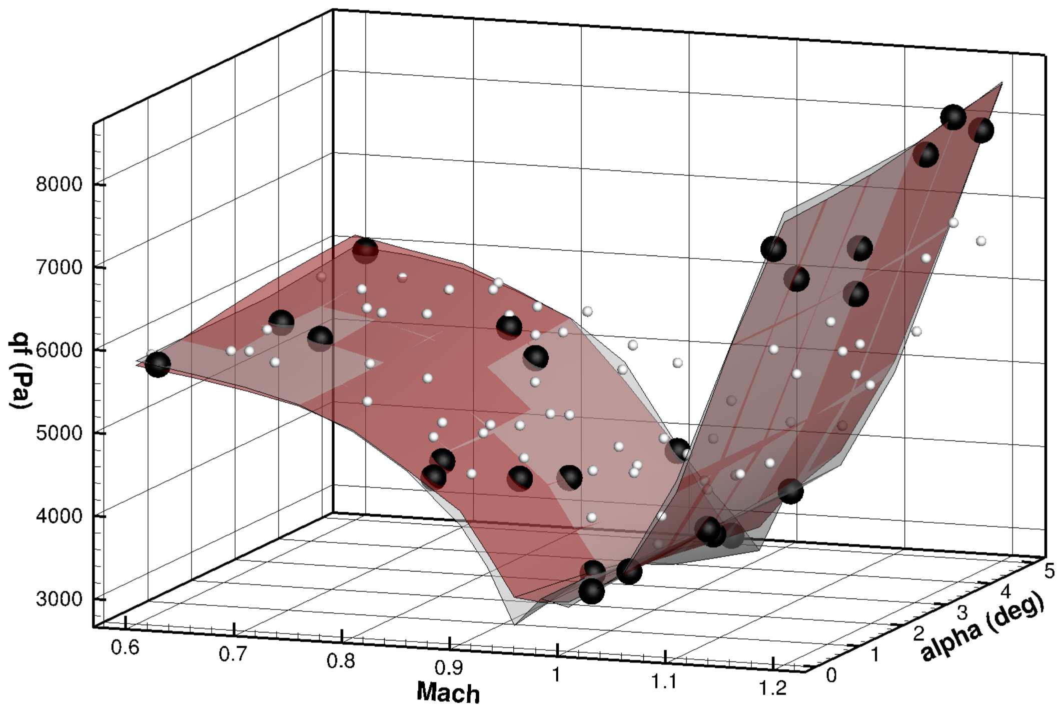

Figure 6: Two-dimensional exact (white) and MFS kriging model (red). High-fidelity training points are shown as black and low-fidelity ones as white spheres.

Figure 7 shows the quantitative performance with and without the enhancement via low-fidelity data. One can observe that the MFS models yield more accurate results compared to using high-fidelity data alone (compare black to red and green lines) even when the cost for obtaining the lower-fidelity samples is taken into account. This is especially true at the beginning of the simulation. The poorer performance at the end is likely due to over-fitting.

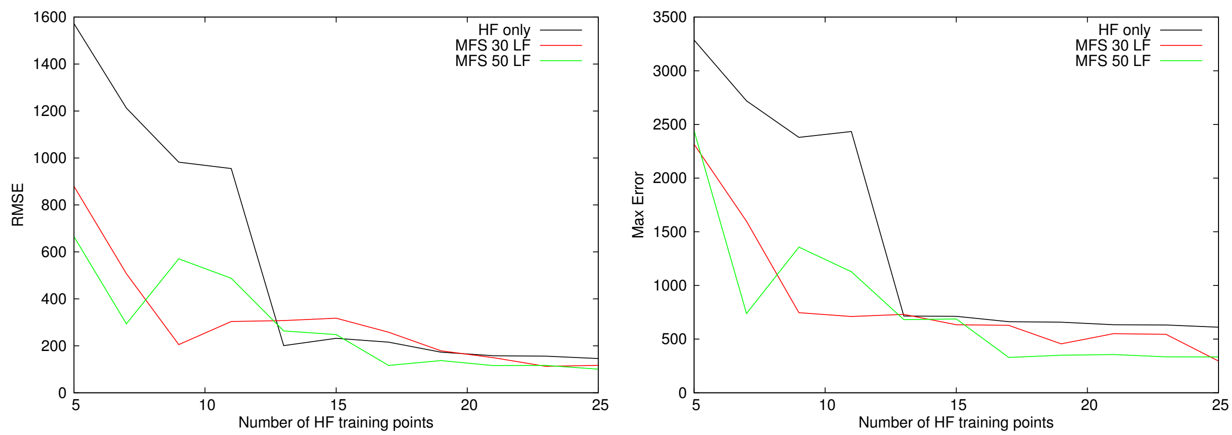

Figure 7: RMSE (left) and maximum error (right) for kriging surrogate enhanced with low-fidelity data as a function of number of high-fidelity training points in two dimensions.

3.2 Three-dimensional MFS Models

Figure 8 shows isosurfaces of all three fidelity level simulation results for q_f as a function of Mach number, angle of attack and thickness to chord ratio. For the HF data a Cartesian mesh of $13 \times 2 \times 5 = 130$ nodes

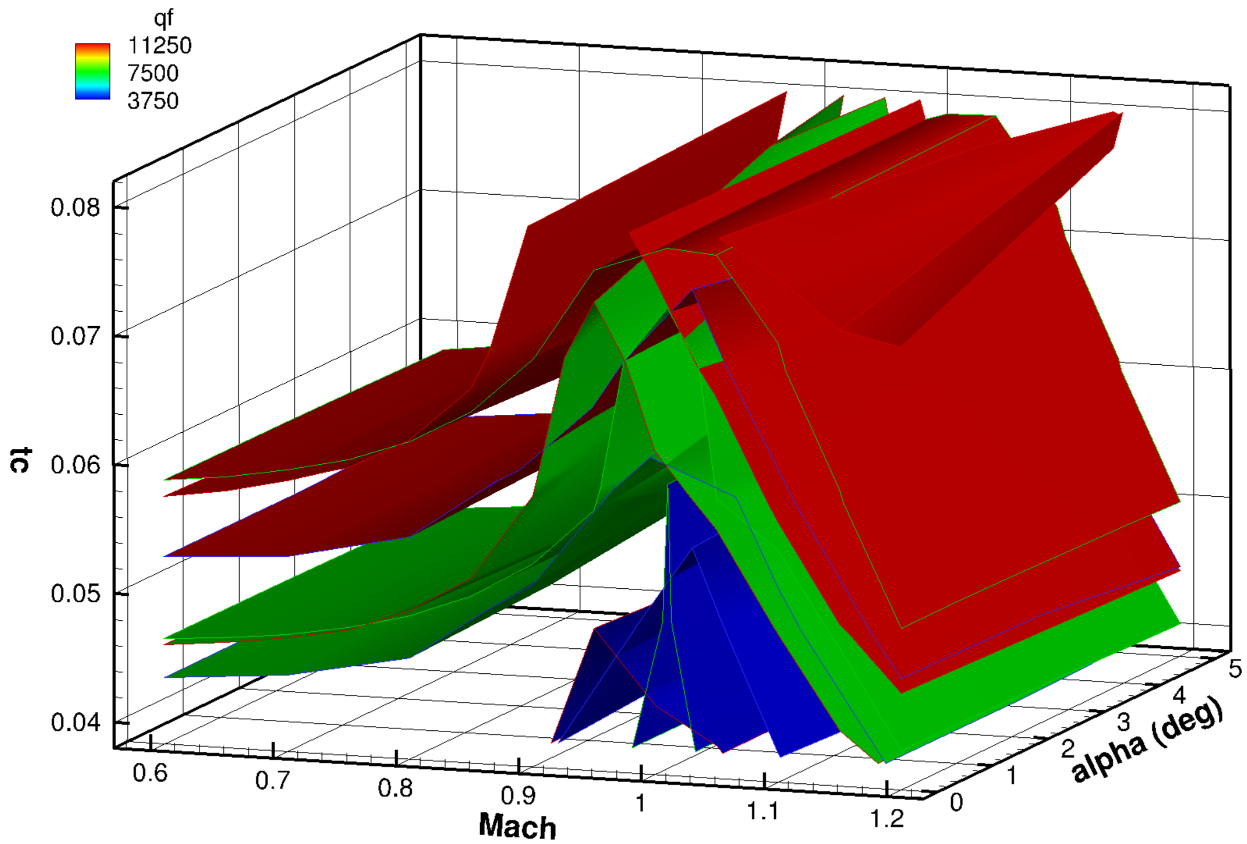

Figure 8: AGARD 445.6 flutter design space with three inputs. The green, blue and red edges are ASTROS, ZEUS, and inviscid Fun3D results, respectively. Shown are three isosurfaces with $q_f = 3750\,Pa$, $q_f = 7500\,Pa$ and $q_f = 11250\,Pa$.

is employed. One can see that the low-fidelity trends match the high-fidelity ones which is encouraging for the use of a multi-fidelity approach.

All three-dimensional MFS models started with the same nine HF training points (8 corners and center of domain). Then the adaptive training point framework added three HF training points per iteration until a maximum amount (33) was reached. When lower fidelity data was used the initial LF locations coincided again with all the HF training points and the remaining LF points were picked via latin hypercube sampling subject to a distance constraint. Also, whenever a HF point is added via the dynamic training point algorithm the corresponding lower fidelity point is added to the set as well. Here, 50, 75, 100 and 150 low-fidelity starting points were employed.

Figure 9 shows the exact and MFS kriging model at the end of a simulation (using 33 HF and 124 LF points). It can be inferred that the MFS model is in good agreement with the exact model and is able to capture the transonic dip behavior very well, demonstrating its ability to model non-smooth functions. One can also observe that the dynamic training point selection clustered HF points in the more varying transonic region as opposed to the relatively flat supersonic and subsonic regions.

Figure 10 shows the quantitative performance with and without the enhancement of low-fidelity data. One can observe that the MFS models yield more accurate results compared to using high-fidelity data alone (compare black to other lines) even when the cost for obtaining the lower-fidelity samples is taken into

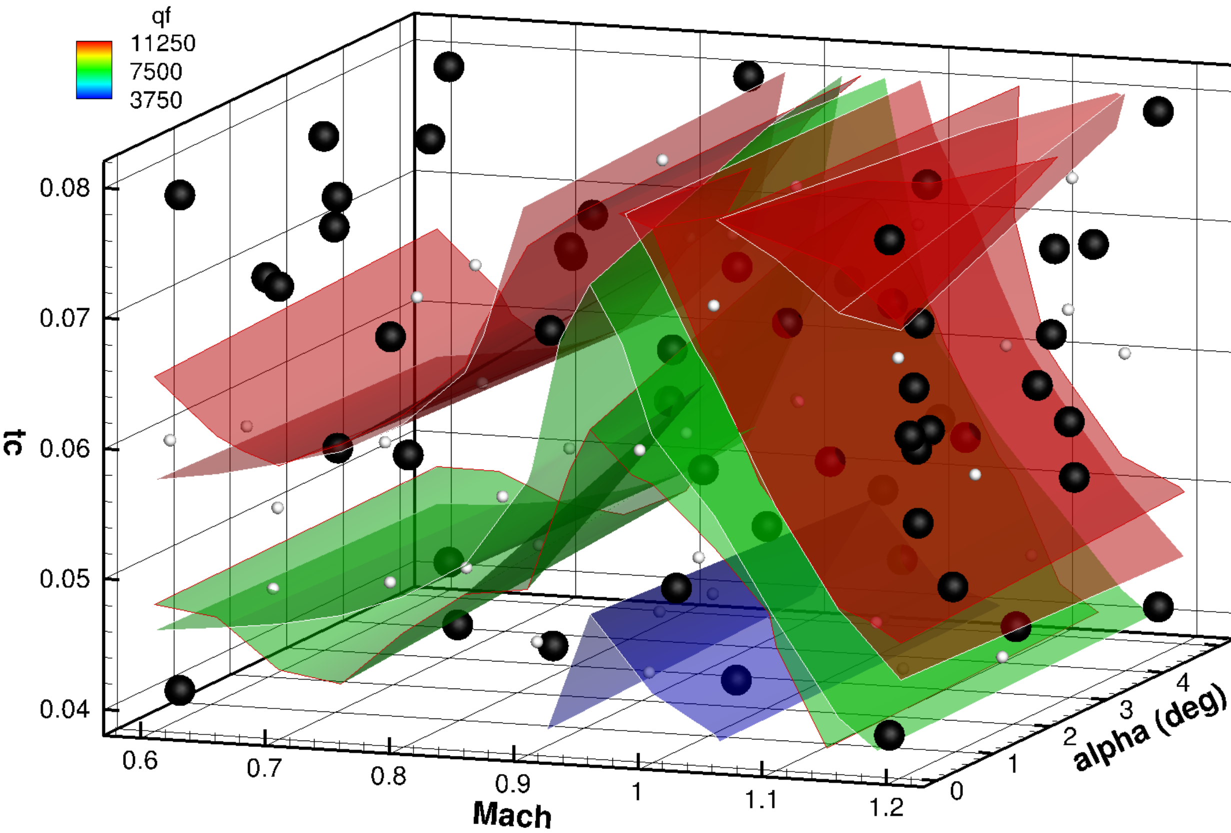

Figure 9: Three-dimensional exact (white edges) and MFS kriging model (red edges). High-fidelity training points are shown as black and low-fidelity ones as white spheres.

account. This is especially true at the beginning of the simulation. The poorer performance at the end is again likely due to over-fitting.

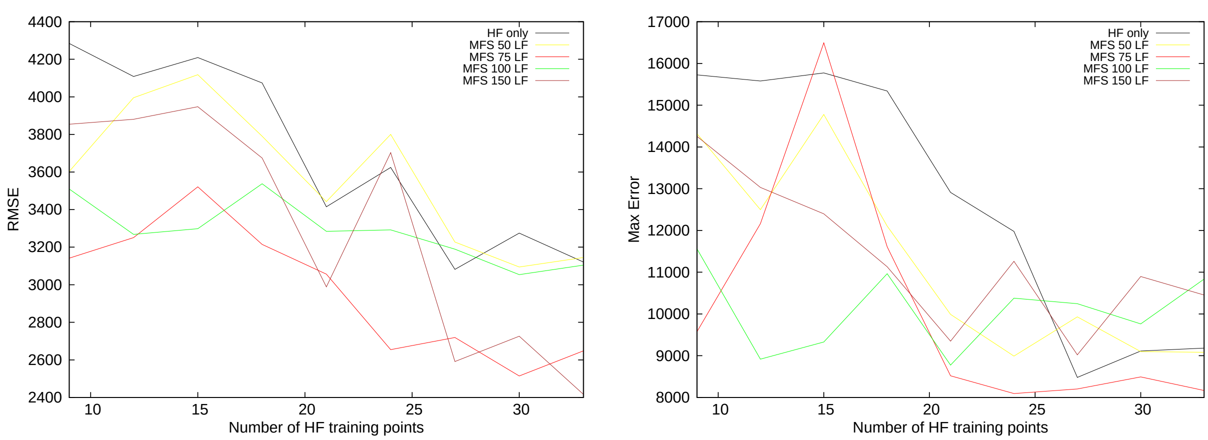

Figure 10: RMSE (left) and maximum error (right) for kriging surrogate enhanced with low-fidelity data as a function of number of high-fidelity training points in three dimensions.

3.2.1 Three Fidelity Levels

Figure 11 shows the exact and MFS kriging model built using three fidelity levels at the end of a simulation (using 33 HF, 44 MF, and 74 LF points). It can be inferred that the MFS model is in relatively good agreement with the exact model, however, it is not quite able to capture the transonic dip behavior. One can also observe that the dynamic training point selection clustered HF points in the more varying transonic region as opposed to the relatively flat subsonic region.

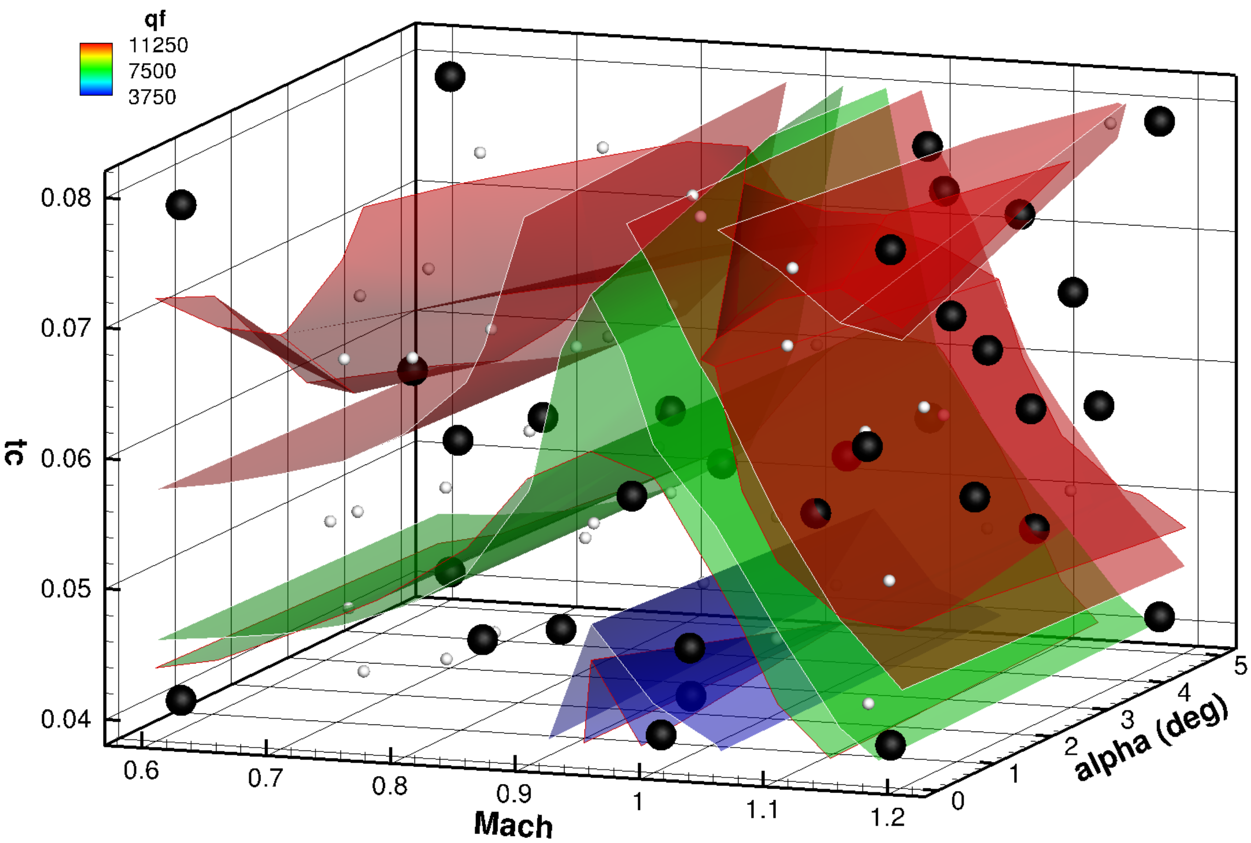

Figure 11: Three-dimensional exact (white edges) and MFS kriging model built with three fidelity levels (red edges). High-fidelity training points are shown as black and lower fidelity ones as white spheres.

Figure 12 shows the quantitative performance with and without the enhancement of medium- and low-fidelity data. One can observe that the MFS models yield more accurate results compared to using high-fidelity data alone. Overall, the best performing simulations utilizes 20 MF and 50 LF training points at the beginning.

4 Conclusion

This paper has presented multi-fidelity surrogate (MFS) models of critical flutter dynamic pressures for the AGARD 445.6 aeroelastic test case model as a function of Mach number, angle of attack and thickness to chord ratio. Up to three fidelity levels for the analysis were considered. The highest fidelity level were body fitted Euler flow solutions, the medium level were transpiration boundary Euler aerodynamics, and the lowest level were panel solutions, all combined with the same modal structural solver. Fairly accurate surrogate models of the flutter database could be constructed using only 30 or so high-fidelity Euler training points. Overall, the MFS models yield more accurate results compared to using high-fidelity data alone especially at the beginning of the simulation when only a handful HF data points are available.

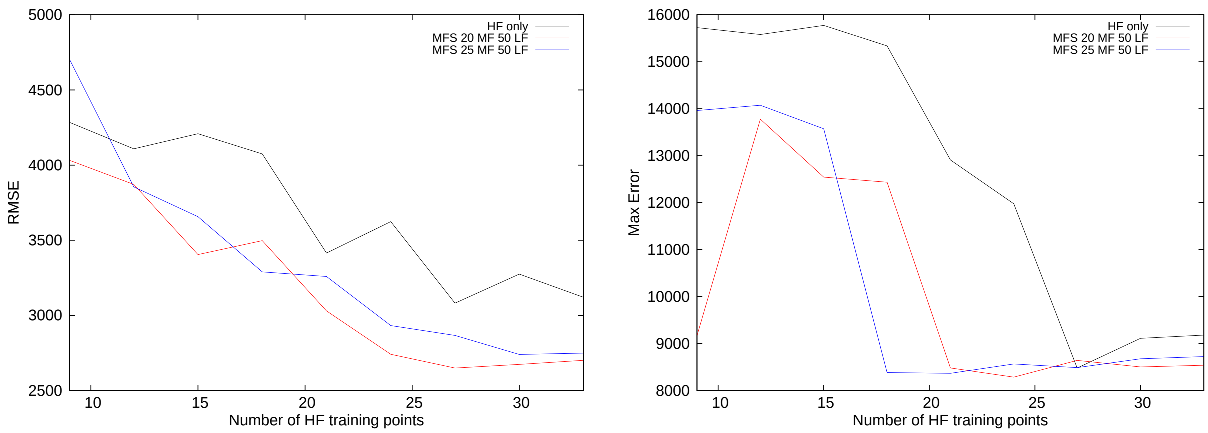

Figure 12: RMSE (left) and maximum error (right) for kriging surrogate enhanced with medium- and low-fidelity data as a function of number of high-fidelity training points in three dimensions.

Acknowledgments

The second author acknowledges support of the US Air Force Office of Scientific Research (grant 17RQCOR473, Dr. Jean-Luc Cambier, Computational Mathematics Program Officer).

References

[1] O. O. Bendiksen. Transonic Limit Cycle Flutter of High-Aspect-Ratio Swept Wings. *Journal of Aircraft*, 45, No. 5:1522–1533, 2008.

[2] O. O. Bendiksen. High-Altitude Limit Cycle Flutter of Transonic Wings. *Journal of Aircraft*, 46, No. 1:123–136, 2009.

[3] E. Carson Yates, Jr. AGARD Standard Aeroelastic Configurations for Dynamic Response I - Wing 445.6. Technical Report AGARD 765, 1988.

[4] D. G. Krige. A statistical approach to some basic mine valuations problems on the Witwatersrand. *Journal of the Chemical Metallurgical and Mining Engineering Society of South Africa*, 52 (6):119–139, 1951.

[5] N. Cressie. The Origins of Kriging. *Mathematical Geology*, 22, No. 3:239–252, 1990.

[6] J. R. Koehler and A. B. Owen. Computer Experiments. In *Handbook of Statistics, Ghosh, S., Rao, C.R., (Eds.)*. pp. 261-308, 1996.

[7] W. Yamazaki, S. Mouton, and G. Carrier. Efficient Design Optimization by Physics-Based Direct Manipulation Free-Form Deformation. AIAA Paper, 2008-5953, 2008.

[8] M. P. Rumpfkeil, W. Yamazaki, and D. J. Mavriplis. Uncertainty Analysis Utilizing Gradient and Hessian Information. Sixth International Conference on Computational Fluid Dynamics, ICCFD6, St. Petersburg, Russia, July, 2010.

[9] H. S. Chung and J. J. Alonso. Using Gradients to Construct Cokriging Approximation Models for High-Dimensional Design Optimization Problems. AIAA Paper, 2002-0317, 2002.

[10] J. Laurenceau and P. Sagaut. Building Efficient Response Surfaces of Aerodynamic Functions with Kriging and Cokriging. *AIAA Journal*, 46, No. 2:498–507, 2008.

[11] J. Laurenceau and M. Meaux. Comparison of Gradient and Response Surface Based Optimization Frameworks Using Adjoint Method. AIAA Paper, 2008-1889, 2008.

[12] W. Yamazaki, M. P. Rumpfkeil, and D. J. Mavriplis. Design Optimization Utilizing Gradient/Hessian Enhanced Surrogate Model. AIAA Paper, 2010-4363, 2010.

[13] M. P. Rumpfkeil, W. Yamazaki, and D. J. Mavriplis. A Dynamic Sampling Method for Kriging and Cokriging Surrogate Models. AIAA Paper, 2011-883, 2011.

[14] K. Boopathy and M. P. Rumpfkeil. A Unified Framework for Training Point Selection and Error Estimation for Surrogate Models. *AIAA Journal*, 53:215–234, 2015.

[15] Z. H. Han, R. Zimmermann, and S. Goertz. On Improving Efficiency and Accuracy of Variable-Fidelity Surrogate Modeling in Aero-data for Loads Context. CEAS 2009 European Air and Space Conference, 2009.

[16] Z. H. Han, R. Zimmermann, and S. Goertz. A New Cokriging Method for Variable-Fidelity Surrogate Modeling of Aerodynamic Data. AIAA Paper, 2010-1225, 2010.

[17] W. Yamazaki and D. J. Mavriplis. Derivative-Enhanced Variable Fidelity Surrogate Modeling for Aerodynamic Functions. AIAA Paper, 2011-1172, 2011.

[18] Z. H. Han, S. Goertz, and R. Zimmermann. Improving variable-fidelity surrogate modeling via gradient-enhanced kriging and a generalized hybrid bridge function. *Aerospace Science and Technology*, 25, No. 1:177–189, 2013.

[19] D. L. Clark and H.-R. Bae. Engineering Design Exploration Utilizing Locally-Optimized Covariance Kriging. AIAA Paper, 2015-1372, 2015.

[20] D. L. Clark, H.-R. Bae, K. Gobal, and R. Penmetsa. Engineering Design Exploration utilizing Locally Optimized Covariance Kriging. *AIAA Journal*, 54, No. 10:3160–3175, 2016.

[21] R. P. Liem, C. A. Mader, and J. R. R. A. Martins. Surrogate models and mixtures of experts in aerodynamic performance prediction for aircraft mission analysis. *Aerospace Science and Technology*, 43:126–151, 2015.

[22] M. P. Rumpfkeil and P. Beran. Construction of Multi-Fidelity Surrogate Models for Aerodynamic Databases. Proceedings of the Ninth International Conference on Computational Fluid Dynamics, ICCFD9, Istanbul, Turkey, July 11-15, 2016.

[23] M. P. Rumpfkeil, K. Hanazaki, and P. Beran. Construction of Multi-Fidelity Locally Optimized Surrogate Models for Uncertainty Quantification. AIAA Paper, 2017-1948, 2017.

[24] M. P. Rumpfkeil and P. Beran. Construction of Dynamic Multi-Fidelity Locally Optimized Surrogate Models. *AIAA Journal*, 55, No. 9:3169–3179, 2017.

[25] E. Alyanak, R. Durscher, R. Haimes, J. F. I. Dannenhoffer, N. Bhagat, and D. Allison. Multi-fidelity, Gemoetry-centric Multi-disciplinary Analysis for Design. AIAA Paper, 2016-4007, 2016.

[26] D. L. Marcum and N. P. Weatherill. Unstructured Grid Generation Using Iterative Point Insertion and Local Reconnection. *AIAA Journal*, 33 No. 9:1619–1625, 1995.

[27] D. L. Marcum. *Unstructured Grid Generation Using Automatic Point Insertion and Local Reconnection*. The Handbook of Grid Generation, edited by J.F. Thompson, B. Soni, and N.P. Weatherill, CRC Press, 1998.

[28] E. H. Johnson and V. B. Venkayya. Automated structural optimization system (ASTROS) Volume I - Theoretical manual. Technical Report AFWAL-TR-88-3028, Air Force Wright Aeronautical Laboratories, 1988.

[29] R. L. Harder and R. N. Desmarais. Interpolation using Surface Splines. *Journal of Aircraft*, 9 No. 2:189–191, 1972.

[30] E. Albano and W. P. Rodden. A Doublet-Lattice Method for Calculating Lift Distributions on Oscillating Surfaces in Subsonic Flows. *AIAA Journal*, 7:279–285, 1969.

[31] K. Appa. Constant Pressure Panel Method for Supersonic Unsteady Airloads Analysis. *Journal of Aircraft*, 24:696–702, 1987.

[32] ZONA TECHNOLOGY, INC. ZEUS Version 3.3L User Manual. Technical report, 2013.

[33] R.T. Biedron J. Carlson, J.M. Derlaga, P.A. Gnoffo, D.P. Hammond, W.T. Jones, B. Kleb, E. Lee-Rausch, E.J. Nielsen, M.A. Park, C.L. Rumsey, J.L. Thomas, and W.A. Wood. FUN3D Manual: 12.7. NASA Technical Memorandum 218761, 2015.

[34] R. T. Biedron and J. L. Thomas. Recent Enhancements to the FUN3D Flow Solver for Moving-Mesh Applications. AIAA Paper, 2009-1360, 2009.